LETTER **Communicated by Emilio Salinas**

Assessing Neuronal Coherence with Single-Unit, Multi-Unit, and Local Field Potentials

Magteld Zeitler
m.zeitler@science.ru.nl
Department of Medical Physics and Biophysics, Institute for Neuroscience, Radboud University Nijmegen, 6525 EZ Nijmegen, Netherlands

Pascal Fries
pascal.fries@fcdonders.ru.nl
F. C. Donders Centre for Cognitive Neuroimaging and Department of Biophysics, Institute for Neuroscience, Radboud University Nijmegen, 6525 EZ Nijmegen, Netherlands

Stan Gielen
s.gielen@science.ru.nl
Department of Medical Physics and Biophysics, Institute for Neuroscience, Radboud University Nijmegen, 6525 EZ Nijmegen, Netherlands

The purpose of this study was to obtain a better understanding of neuronal responses to correlated input, in particular focusing on the aspect of synchronization of neuronal activity. The first aim was to obtain an analytical expression for the coherence between the output spike train and correlated input and for the coherence between output spike trains of neurons with correlated input. For Poisson neurons, we could derive that the peak of the coherence between the correlated input and multi-unit activity increases proportionally with the square root of the number of neurons in the multi-unit recording. The coherence between two typical multi-unit recordings (2 to 10 single units) with partially correlated input increases proportionally with the number of units in the multi-unit recordings. The second aim of this study was to investigate to what extent the amplitude and signal-to-noise ratio of the coherence between input and output varied for single-unit versus multi-unit activity and how they are affected by the duration of the recording. The same problem was addressed for the coherence between two single-unit spike series and between two multi-unit spike series. The analytical results for the Poisson neuron and numerical simulations for the conductance-based leaky integrate-and-fire neuron and for the conductance-based Hodgkin-Huxley neuron show that the expectation value of the coherence function does not increase for a longer duration of the recording. The only effect of a longer duration of the spike recording is a reduction of the noise in the

coherence function. The results of analytical derivations and computer simulations for model neurons show that the coherence for multi-unit activity is larger than that for single-unit activity. This is in agreement with the results of experimental data obtained from monkey visual cortex (V4). Finally, we show that multitaper techniques greatly contribute to a more accurate estimate of the coherence by reducing the bias and variance in the coherence estimate.

1 Introduction

The recent advent of multiple electrode recording technology makes it possible to study the simultaneous spiking activity of many neurons. This allows us to explore how stimuli are encoded by neuronal activity and how groups of neurons act in concert to define the function of a given brain region. However, in spite of the considerable technological developments and the advanced analysis tools (for an overview, see Brown, Kass, & Mitra, 2004), there are many fundamental questions regarding the interpretation of multi-unit activity.

The gold standard in animal neurophysiology has been thought to be the study of isolated single units for a long time. However, it appears as if the use of measures of neuronal aggregate activity, like multi-unit or local field potential recordings, greatly enhances the sensitivity of correlation and coherence analyses (see, e.g., Baker, Pinches, & Lemon, 2003; Rolls, Franco, Aggelopous, & Reece, 2003). This empirical observation is not yet understood. Related to this is the question whether a multi-unit recording for time T and consisting of m single units with the same correlated input carries the same information as a single-unit recording for time mT.

Many studies (see, e.g., Singer & Gray, 1995; Kreiter & Singer, 1996; Engel, Fries, & Singer, 2001; Fries, Neuenschwander, Engel, Goebel, & Singer, 2001) have so far demonstrated that neurons in early and intermediate visual cortex in cat and macaque exhibit significant correlated fluctuations in their responses to visual stimuli. These cells undergo attention-modulated fluctuations in excitability that enhance temporal coherence of the responses to visual stimuli (Fries, Reynolds, Rorie, & Desimone, 2001; Fries, Schröder, Roelfsema, Singer, & Engel, 2002). The coherence is an important parameter, since it provides a measure for the similarity between two signals. Moreover, coherence among subthreshold membrane potential fluctuations likely expresses functional relationships during states of expectancy or attention, allowing the grouping and selection of distributed neuronal responses for further processing (Fries, Neuenschwander, et al., 2001). The coherence between spike activity and local field potential was larger for multi-unit activity than for single-unit activity. Along the same lines, Baker et al. (2003) studied the cross-correlation and coherence between local field potentials and neural spike trains in monkey primary motor cortex. They concluded that a (small) population of neurons is necessary to encode effectively the

cortical oscillatory signal, that is, the rapid modulations of synaptic input reflected in the oscillatory local field potential.

Several studies reported a lack of evidence for synchronized neuronal activity. For example, Tovee and Rolls (1992), in the inferior temporal visual cortex, and Luck, Chelazzi, Hillyard, and Desimone (1997) did not observe clear synchronization in neuronal responses in V2 and V4. However, Kreiter and Singer (1996) did find clear synchronization in the middle temporal area (MT) if two cells were activated by the same stimulus. Besides recording in different recording areas and the use of different types of stimuli, the statistical analysis technique might also play an important role in detecting synchronization. Advanced multitaper techniques (Percival & Walden, 2002) have proven to be useful in estimating coherence between spike trains and local field potentials by improving the signal-to-noise ratio (Pesaran, Pezaris, Shahani, Mitra, & Andersen, 2002; see also Jarvis & Mitra, 2001). These multitaper techniques improved the significance of synchronized oscillatory neuronal activity.

The aim of this study was threefold. First, we wanted to obtain a quantitative understanding of the interpretation of correlated output spike trains in terms of correlated input (indirectly related to the local field potential) to the neurons. In order to do so, we started with a network of simple Poisson neurons, the behavior of which could be analyzed analytically. This simple model was then made more realistic by replacing the Poisson neurons by conductance-based neurons. The second aim of this study was to investigate to what extent the shape, amplitude, and signal-to-noise ratio of the coherence between input and output varied for single-unit versus multi-unit activity and whether the recording of single-unit activity over a long period of time could produce the same cross-correlation and coherence with local field potential as multi-unit activity over a shorter period of time. We addressed the same question for the coherence between two spike outputs for both two single-unit and two multi-unit spike series. The third aim of this study was to investigate the effectiveness of analysis techniques in revealing coherent activity in multi-unit activity. These three topics were investigated by comparing the results of coherence for single-unit and multi-unit activity in theoretical analyses for Poisson neurons, in computer simulations for conductance-based model neurons, and for data measured in monkey visual cortex (V4) (Fries, Reynolds, et al., 2001).

2 Methods and Theory

In order to obtain better insight into the coherence between the local field potential (LFP) at the one hand and single-unit or multi-unit activity at the other hand and in the coherence between spike trains of neurons that receive partially correlated input, we will start with a simple model (see

Figure 1). The local field potential reflects mainly the sum of postsynaptic potentials from local cell groups (Buzsáki, 2004). Therefore, the local field potential is seen to be indirectly related to the correlated input of neurons. We consider groups of neurons receiving correlated input that is reflected in a simulated LFP. We therefore modeled those neurons as rate-varying Poisson processes with a baseline firing rate plus rate modulations driven by the LFP fluctuations. Note that in this study, we refer to the LFP as common rate fluctuations of the input signal (for short, common input). In order to prevent any misunderstanding, we would like to point out that this meaning of *common input* differs from the usual physiological meaning of common input, which implies that two neurons receive the same synaptic input due to a bifurcating axon.

In this study, we will determine the coherence between different signals present in the model, as shown in Figure 1. First, we concentrate on the Poisson model and derive an expression for the coherence between the common input (LFP) and the response of a single Poisson neuron (the small circle in Figure 1). After deriving a similar expression for multi-unit activity, we compare both results of spike-field coherence functions. We finish the theoretical part, concerning the coherence functions, by deriving expressions for the spike-spike coherences, first between two single-unit activities and later between two multi-unit series of Poisson neurons. Simulation results of these coherence measures will complete the Poisson model section. We continue by simulations of the complete model, including the conductance-based neurons (the large circles in Figure 1). The common input (LFP) to the Poisson neurons will be taken as the local field potential in order to determine the spike-field coherences between the common input and the response(s) of the conductance-based neuron(s). The spike-spike coherences are taken between the responses of two conductance-based neurons (single-units) and then between the sums of 10 responses (multi-units) of this neuron type. We finish with the coherence analysis of experimental data.

2.1 Poisson Model and Coherences. In the simple model in Figure 1, we feed Poisson neurons with partially common rate fluctuations $N_c\sigma\eta_0(t)$ and uncorrelated noise $(1 - N_c)\sigma\eta_i(t)$ (as described below), in order to translate the LFP into a series of (partially) correlated spike trains. For this part of the model, we derive analytical expressions for the coherence between LFP and single-unit or multi-unit activity and for the coherence between spike trains. The spike output of the Poisson neurons is fed into a set of neurons, which could be conductance-based leaky integrate-and-fire neurons or conductance-based Hodgkin-Huxley neurons.

The Poisson neurons each receive an input

$$x_i(t) = \lambda + N_c\sigma\eta_0(t) + (1 - N_c)\sigma\eta_i(t) \tag{2.1}$$

with a constant input λ, gaussian colored noise η_0, and gaussian white noise η_i, with $< \eta_i(t)\eta_j(t+\tau) >= \delta_{ij}(\tau)$. The common input ratio N_c varies from zero (uncorrelated input to all neurons) to one (the same input to all neurons). Both $\eta_0(t)$ and $\eta_i(t)$ have zero mean and a variance of one. In this study, σ is set to $\lambda/3$, so the total input to the neurons is always positive and, therefore, the probability that a spike occurs too.

Experiments in visual cortex (Fries, Neuenschwander, et al., 2001; Fries, Reynolds, et al., 2001; Fries et al., 2000) have shown that the local field potential, which represents a measure of the local correlated input to a group of neurons (Buzsáki et al., 2004), has a peak in the power spectrum in the range between 40 and 60 Hz. Therefore, we used bandpass-filtered gaussian white noise $\eta_0(t)$ as a time-dependent common rate fluctuation, which was obtained by filtering gaussian white noise with a bandpass filter with 3 dB points at 45 and 55 Hz and a quality factor Q of 5.

The response of Poisson neuron i to the input $x_i(t)$ is represented by a sequence of action potentials $y_i(t) = \sum_j \delta(t - t_j^i)$, where t_j^i represents the occurrence time of the jth spike of neuron i. In this study, we introduce a discretization of time in bins Δt of 1 ms, such that $y_i(t) = 1$ for an action potential in the time interval $[t, t + \Delta t)$ with probability $x_i(t)\Delta t$ and with $y_i(t) = 0$ with probability $(1 - x_i(t)\Delta t)$. Multi-unit activity is defined as the sum of m single-unit activities $z(t) = \sum_{i=1}^{m} \sum_j \delta(t - t_j^i)$.

A commonly used measure to estimate the relation between input $x(t)$ and output $y(t)$ of a neuron is the normalized cross-covariance function

Figure 1: Schematic overview of the network of neurons for the simulations. A set of Poisson neurons receives common rate fluctuations (local field potential) and uncorrelated input to generate a set of correlated spike trains. These spike trains provide the input for a set of neurons, which are modeled as leaky integrate-and-fire (LIF) neurons or Hodgkin-Huxley (HH) neurons. A population of Poisson neurons is represented by an oval with small circles. Each Poisson neuron receives a common input given by $\lambda + N_c\sigma\eta_o(t)$ and a unique input given by $(1 - N_c)\sigma\eta_{ij}(t)$, which is uncorrelated in time and space. λ is a constant, η_0 represents the common rate fluctuations to the Poisson neurons and is represented by bandpass filtered gaussian white noise, and η_{ij} is gaussian white noise for the jth Poisson neuron of the ith population. *Poisson model:* Only one population of 20 Poisson neurons is used for the Poisson model. $y_i(t)$ represents the single-unit activity of Poisson neuron i, multi-unit activity is the sum of the responses of 10 neurons. *LIF (HH) model*: Each of the 20 LIF (HH) neurons (large circle) receives input from one of the 20 populations with 100 Poisson neurons each (oval). Single-unit activity is the response of one conductance-based neuron; multi-unit activity is the sum of 10 single-unit activities.

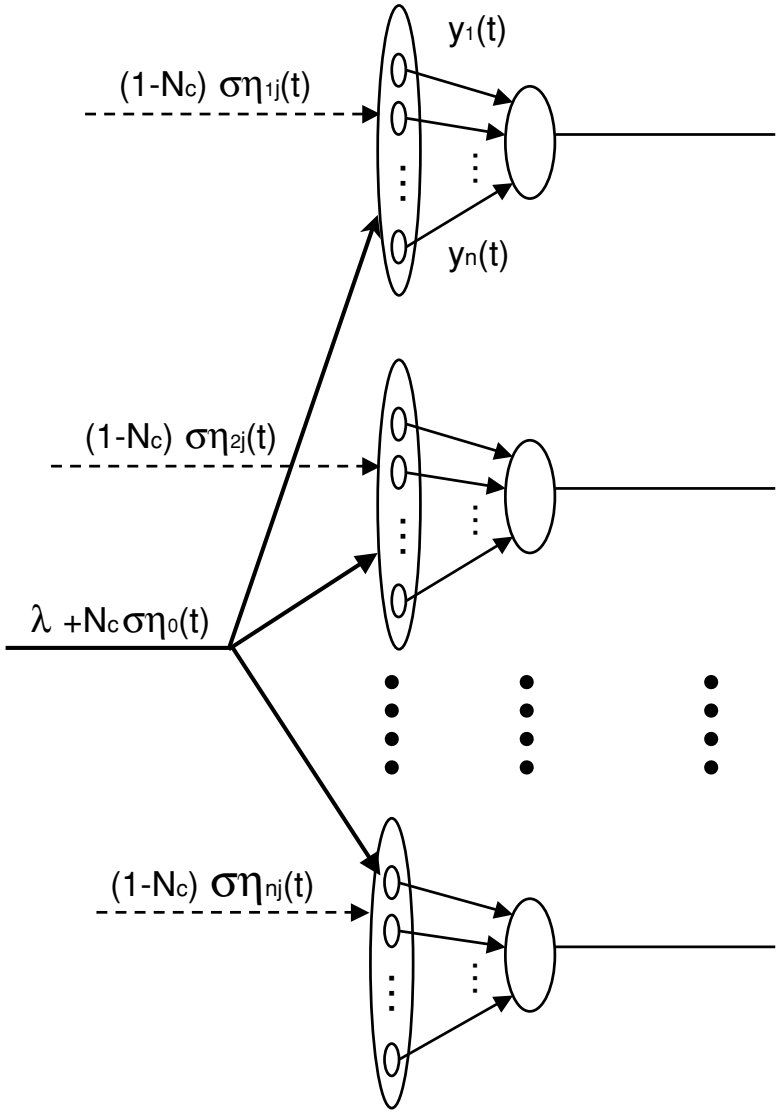
$y_1(t)$
$(1-N_c)\ \sigma\eta_{1j}(t)$
$y_n(t)$
$(1-N_c)\ \sigma\eta_{2j}(t)$
$\lambda + N_c\sigma\eta_0(t)$
$(1-N_c)\ \sigma\eta_{nj}(t)$

or correlation coefficient function, which is defined by (Marmarelis & Marmarelis, 1978),

$$\rho_{xy}(\tau) \equiv \frac{C_{xy}(\tau)}{\sqrt{C_{xx}(0)C_{yy}(0)}} \tag{2.2}$$

with the cross-covariance function between two ergodic signals x and y defined as

$$C_{xy}(\tau) = \int\int x(t+\tau)\, y(t)\, p(x(t+\tau), y(t))\, dx(t+\tau)dy(t) - \overline{x}\,\overline{y}, \tag{2.3}$$

where $p(x(t+\tau), y(t))$ is the joint probability distribution of $x(t+\tau)$ and $y(t)$ and where $\overline{x}$ and $\overline{y}$ represent the averaged value of signal x and y, respectively.

The coherence function $\gamma(\omega)$ reflects how much of the variation in the output y can be attributed to a linear filtering of the input signal x. The coherence function $\gamma(\omega)$ is defined by

$$\mid \gamma(\omega) \mid = \frac{\mid C_{xy}(\omega) \mid}{\sqrt{\mid C_{xx}(\omega) \mid}\sqrt{\mid C_{yy}(\omega) \mid}}. \tag{2.4}$$

The coherence takes values in the range between 0 (input and output are fully uncorrelated) and 1 (the output is equal to the input after convolution by a linear system).

First, we determine the coherence between the single-unit activity of a Poisson neuron and the common rate fluctuations by deriving expressions for the covariance functions in the denominator and the cross-covariance function in the numinator of equation 2.4.

Consider $x(t)$ to be the input given by equation 2.1 and $y_i(t) = y(t)$ the response of a single Poisson neuron. Each Poisson neuron is represented by a small circle in Figure 1. The covariance function of the input is given by

$$\begin{aligned} C_{xx}(\tau) &= \int\int x(t)x(t+\tau)p(x(t), x(t+\tau))dx(t)dx(t+\tau) \\ &= \int\int\int\int x(t)x(t+\tau)p(\eta_0(t), \eta_0(t+\tau))p(\eta_i(t), \eta_i(t+\tau)) \\ &\quad d\eta_0(t)d\eta_0(t+\tau)d\eta_i(t)d\eta_i(t+\tau) - \overline{x}^2 \\ &= N_c^2\sigma^2\rho(\tau) + (1-N_c)^2\sigma^2\delta(\tau), \end{aligned} \tag{2.5}$$

where the joint probability distributions for $\tau \neq 0$ are given by

$$p(\eta_0(t+\tau), \eta_0(t)) = \frac{1}{2\pi\sqrt{1-\rho^2(\tau)}} \exp\left(-\frac{\eta_0^2(t+\tau) - 2\rho(\tau)\eta_0(t+\tau)\eta_0(t) + \eta_0^2(t)}{2(1-\rho^2(\tau))}\right)$$

$$p(\eta_i(t+\tau), \eta_i(t)) = p(\eta_i(t))p(\eta_i(t+\tau), \tag{2.6}$$

with $\rho(\tau) = \rho_{\eta_0\eta_0}(\tau)$ being the normalized covariance function of the gaussian colored noise η_0. In order to obtain equation 2.5, we used for the common input colored noise $\eta_0(t)$ and for the uncorrelated noise $\eta_i(t)$ in the input signal $x(t)$ defined in equation 2.1 for $\tau = 0$:

$$\begin{aligned}\int \eta_o(t+\tau)p(\eta_0(t+\tau), \eta_0(t) \mid \tau)d\eta_0(t+\tau) &= \eta_0(t)\ p(\eta_0(t)) \\ &= \frac{\eta_0(t)}{\sqrt{2\pi}} \exp\left(-\frac{\eta_0^2(t)}{2}\right) \\ \int \eta_i(t+\tau)p(\eta_i(t+\tau), \eta_i(t) \mid \tau)\, d\eta_i(t+\tau) &= \eta_i(t)\ p(\eta_i(t)) \\ &= \frac{\eta_i(t)}{\sqrt{2\pi}} \exp\left(-\frac{\eta_i^2(t)}{2}\right),\end{aligned} \tag{2.7}$$

The first term on the right-hand side of equation 2.5 is due to the common rate fluctuations to the neurons, and the second term due to the neuron-specific input fluctuations.

The covariance function of a single-unit response results in

$$\begin{aligned}C_{yy}(\tau) &= p(y(t+\tau) = 1, y(t) = 1) - \overline{y}^2 \\ &= \int\int\int\int p(y(t+\tau) \\ &= 1 \mid \eta_0(t+\tau), \eta_i(t+\tau))p(y(t) = 1 \mid \eta_0(t), \eta_i(t))p(\eta_0(t), \\ &\quad \eta_0(t+\tau))p(\eta_i(t), \eta_i(t+\tau))d\eta_0(t)d\eta_0(t+\tau)d\eta_i(t) \\ &\quad \times d\eta_i(t+\tau) - \overline{y}^2 \\ &= \Delta t^2\sigma^2 N_c^2(\rho(\tau) - \delta(\tau)) + \Delta t\lambda(1 - \Delta t\lambda)\delta(\tau),\end{aligned} \tag{2.8}$$

where ρ is the normalized covariance function of the gaussian colored noise.

The cross-covariance function between the input x and the single-unit response y is given by

$$\begin{aligned} C_{xy}(\tau) &= \int x(t+\tau)p(x(t+\tau), y(t)=1 \mid \tau)dx(t+\tau) - \overline{xy} \\ &= \Delta t\sigma^2 N_c^2 \rho(\tau) + \Delta t\sigma^2(1-N_c)^2\delta(\tau). \end{aligned} \tag{2.9}$$

The first term on the right-hand side is due to the common rate fluctuations, and the second term is due to the neuron-specific input fluctuations.

The local field potential is considered to be a measure of the local common rate fluctuation of the neurons near the recording electrode. Therefore, we will take only the contributions of the common rate fluctuations in equations 2.5 and 2.9 into account for determining an analytical expression for the spike-field coherence between single-unit activity and local field potential. The spike-field coherence between the single-unit activity and the common rate fluctuations can be obtained by taking the Fourier transform of equation 2.8 and the first terms on the right-hand side of equations 2.5 and 2.9. This results in

$$\begin{aligned} \left|\gamma_{SpF}^{SU}(\omega)\right| &= \frac{\Delta t\sigma^2 N_c^2 \mid \rho(\omega) \mid}{\sigma N_c \sqrt{\mid \rho(\omega) \mid\mid \Delta t\lambda(1-\Delta t\lambda) + (\Delta t\ \sigma)^2 N_c^2(\rho(\omega)-1) \mid}} \\ &= \frac{\Delta t\sigma N_c \sqrt{\mid \rho(\omega) \mid}}{\sqrt{\mid \Delta t\lambda(1-\Delta t\lambda) + (\Delta t\sigma)^2 N_c^2(\rho(\omega)-1) \mid}} \\ &\approx \frac{\Delta t\sigma N_c}{\sqrt{\Delta t\lambda}} \sqrt{\mid \rho(\omega) \mid}, \end{aligned} \tag{2.10}$$

where $\rho(\omega)$ is the Fourier transform of the normalized covariance function of the colored noise. The approximation in the last step is valid since $(\Delta t\sigma)^2 \ll \Delta t\lambda$.

In order to obtain an expression for the coherence between multi-unit activity and the common rate fluctuations, we have to determine the covariance function of multi-unit activity and the cross-covariance function between multi-unit activity and common rate fluctuations. Since the probability that a neuron fires twice within a time bin Δt is very small ($(\Delta t\lambda)^2 \ll 1$), we take terms only to the second order of Δt into account. For multi-unit activity z, which is the summation over m simultaneously recorded single-unit signals $y_i(t)$ with a common input ratio N_c and for $m << \frac{1}{\Delta t\lambda}$, we find

for the multi-unit covariance function:

$$C_{zz}(\tau) = \sum_{j=0}^{m}\sum_{k=0}^{m} jkp(z(t+\tau) = j, z(t) = k) - \overline{z}^2$$
$$\approx m(\Delta t)^2\sigma^2 N_c^2(m\rho(\tau) - \delta(\tau)) + m\Delta t\lambda(1 - \Delta t\lambda)\delta(\tau). \quad (2.11)$$

The cross-covariance function between multi-unit activity and the total input is given by

$$C_{xz}(\tau) = \sum_{j=0}^{m}\int x(t+\tau)\, jp(x(t+\tau), z(t) = j)dx(t+\tau) - \overline{xz}$$
$$\approx m\Delta t\sigma^2 N_c^2\rho(\tau) + m\Delta t\sigma^2(1 - N_c)^2\delta(\tau). \quad (2.12)$$

Equation 2.12 is equal to equation 2.9 except for the factor m.

Combining equation equation 2.11 and the first term on the right-hand side of equations 2.5 and 2.12 leads to the expression for the spike-field coherence between multi-unit activity and the common rate fluctuations:

$$\left|\gamma_{SpF}^{MU}(\omega)\right| \equiv \frac{|\, C_{xz}(\omega)\,|}{\sqrt{|\, C_{xx}(\omega)\,|}\sqrt{|\, C_{zz}(\omega)\,|}}$$
$$\approx \frac{\Delta t\sigma N_c\sqrt{|\, m\rho(\omega)\,|}}{\sqrt{|\, \Delta t\lambda(1 - \Delta t\lambda) + (\Delta t\sigma)^2 N_c^2(m\rho(\omega) - 1)\,|}}$$
$$\approx \frac{\Delta t\sigma N_c}{\sqrt{\Delta t\lambda}}\sqrt{|\, m\rho(\omega)\,|}. \quad (2.13)$$

The spike-field coherence for multi-unit activity, which is the summation of m single-unit recordings, is equal to that for single-unit activity (see equation 2.10) except for a coefficient $\sqrt{m}$.

We can also calculate the coherence between two single-unit responses or between two multi-unit recordings. The cross-covariance function between two single-unit signals y_1 and y_2 is given by

$$C_{y_1y_2}(\tau) = p(y_1(t+\tau) = 1, y_2(t) = 1) - \overline{y_1y_2}$$
$$= (\Delta t\sigma)^2 N_c^2\rho(\tau). \quad (2.14)$$

The spike-spike coherence between two simultaneously recorded single-unit signals with partly common rate fluctuations is given by

$$|\, \gamma_{SpSp}^{SU}\,| \equiv \frac{|\, C_{y_1y_2}(\omega)\,|}{|\, C_{yy}(\omega)\,|} \quad (2.15)$$

$$= \frac{(\Delta t\sigma)^2 N_c^2 \mid \rho(\omega) \mid}{\Delta t\lambda(1-\Delta t\lambda) + (\Delta t\sigma)^2 N_c^2(\rho(\omega)-1)}$$
$$\approx \frac{(\Delta t\sigma N_c)^2}{\Delta t\lambda} \mid \rho(\omega) \mid,$$

where we used $C_{yy} = C_{y_1 y_1} = C_{y_2 y_2}$.

The cross-covariance function of two multi-unit signals is given by:

$$C_{z_1 z_2}(\tau) = \sum_{j,k=0}^{m} jkp(z_1(t+\tau) = j, z_2(t) = k \mid \tau) - \bar{z}^2$$
$$\approx m^2 N_c^2 (\Delta t\sigma)^2 \rho(\tau). \tag{2.16}$$

The spike-spike coherence between two simultaneously recorded multi-unit signals is given by

$$\mid \gamma_{S_p S_p}^{MU} \mid = \frac{m^2(\Delta t\sigma)^2 N_c^2 \mid \rho(\omega) \mid}{\mid m^2(\Delta t\sigma)^2 N_c^2 \rho(\omega) + m(\Delta t\lambda(1-\Delta t\lambda) - (\Delta t\sigma)^2 N_c^2) \mid}$$
$$\approx \frac{m(\Delta t\sigma)^2 N_c^2 \mid \rho(\omega) \mid}{\mid \Delta t\lambda(1-\Delta t\lambda) + (\Delta t\sigma)^2 N_c^2 (m\rho(\omega)-1) \mid}$$
$$\approx \frac{(\Delta t\sigma N_c)^2}{\Delta t\lambda} m \mid \rho(\omega) \mid. \tag{2.17}$$

Equations 2.15 and 2.17 show that for low firing rates ($\lambda\Delta t << 1$) and for $m << 1/(\lambda\Delta t)$, the expected spike-spike coherence between multi-unit signals is approximately m-times larger than the expected spike-spike coherence between single-unit signals. Equations 2.13 and 2.17 show that the spike-spike coherence is (approximately) the square of the spike-field coherence and thus much smaller.

In summary, for our Poisson model, the spike-field coherence and the spike-spike coherence are larger for multi-unit recordings than for single-unit recordings and the spike-spike coherences are much smaller than the spike-field coherences.

2.2 Conductance-Based LIF Model. Since the simple Poisson model is not very realistic, we will discuss a model where conductance-based leaky integrate-and-fire neurons (LIF) receive spike input from the Poisson neurons. The membrane equation of the neurons is then given by

$$C\frac{dU}{dt} = -I_e(t) - I_l(t), \tag{2.18}$$

with membrane capacitance C, membrane potential U, and excitatory and leak currents I_e and I_l, respectively. These currents are given by

$$I_e(t) = G_e(t)(U(t) - E_e)$$
$$I_l(t) = G_l(U(t) - E_r), \tag{2.19}$$

with the excitatory reversal potential E_e, rest potential E_r, and excitatory (leak) conductance $G_e(t)$ (G_l). The excitatory conductance depends on the recent presynaptic spike times and is modeled by:

$$G_e(t) = \sum_{i=1}^{m} \sum_{k=1}^{k_i^{\max}} g_e(t - t_i^k), \tag{2.20}$$

with t_i^k the time of the kth spike of neuron i and with m the number of input neurons. In this study, the conductivity is modeled by an alpha function:

$$g_e(t) = g_0 \left(\frac{t}{\tau_e}\right) \exp\left(-\frac{t}{\tau_e}\right) \Theta(t). \tag{2.21}$$

Here τ_e denotes the time-to-peak of the conductivity $g_e(t)$. Θ is the Heaviside function. When the membrane potential reaches the threshold U_{thr}, a spike will be generated, and the membrane potential U is reset. Specific values for the LIF model are (Stroeve & Gielen, 2001): membrane capacitance $C =$ 325 pF, threshold potential $U_{thr} = -55$ mV, excitatory reversal potential $E_e = 0$ mV, rest potential $E_r = -75$ mV, leak conductance $G_l = 25$ nS, $g_0 =$ 3.24 nS and $\tau_e = 1.5$ ms.

Each LIF neuron (the large circle in Figure 1) receives input from a population of 100 Poisson neurons (oval), with a spike rate output modulated by a common input ($\lambda + N_c \sigma \eta_0(t)$) and an uncorrelated input ($(1 - N_c)\lambda + \sigma \eta_i(t)$), where $\eta_0(t)$ is gaussian colored noise and $\eta_i(t)$ is gaussian white noise, both with zero mean and variance one. For our simulations, these quantities are chosen as for the Poisson model except for σ, which has been chosen by $\sigma = 20/12$, for $\lambda = 20$. In our simulations, we derived the membrane potential by using Euler integration with a step width of 1 ms.

2.3 Conductance-Based Hodgkin-Huxley Model. The next modification of our simple model in Figure 1 is the replacement of the conductance-

based LIF neurons (circles) by conductance-based Hodgkin-Huxley neurons. These neurons are characterized by the differential equation

$$C\frac{dU}{dt} = -I_{Na}(t) - I_K(t) - I_l(t) - I_e(t), \tag{2.22}$$

where the sodium and potassium currents are given by

$$\begin{aligned} I_{Na}(t) &= g_{Na} m^3 h (U(t) - V_{Na}) \\ I_K(t) &= g_K n^4 (U(t) - V_K), \end{aligned} \tag{2.23}$$

and the leak and excitatory currents are as described before (see equation 2.19). V_{Na} and V_K are the sodium and potassium reversal potentials. The time-varying gate variables m, h, and n are given by the differential equation

$$\frac{dx}{dt} = \frac{x_\infty - x}{\tau_x} \tag{2.24}$$

with $x \epsilon \{m, h, n\}$, $\tau_x = \frac{1}{\alpha_x + \beta_x}$ and $x_\infty = \frac{\alpha_x}{\alpha_x + \beta_x}$. These parameters are expressed by

$$\begin{aligned} \alpha_m &= 0.1 \frac{U + 40}{1 - \exp(-0.1(U + 40))} \\ \beta_m &= 4 \exp(-(U + 65)/18) \\ \alpha_n &= \frac{0.01(U + 55)}{1 - \exp(0.1(U + 55))} \\ \beta_n &= 0.125 \exp(-(U + 65)/80) \\ \alpha_h &= 0.07 \exp(-(U + 65)/20) \\ \beta_h &= \frac{1}{1 + \exp(-0.1(U + 35))}. \end{aligned} \tag{2.25}$$

The typical values of the parameters at 6.3°C for the squid axon are membrane capacitance per unit surface, $C = 1\mu\text{F/cm}^2$; maximum conductance per unit area for the sodium, potassium, and leak currents, $g_{Na} = 120$ mS/cm^2, $g_K = 36$ mS/cm^2, and $G_l = 0.3$ mS/cm^2; excitatory reversal potential, $E_e = 0$ mV; rest potential, $E_r = -75$ mV; sodium reversal potential, $V_{Na} = 50$ mV; and potassium reversal potential $V_K = -77$ mV, $g_0 = 1.5\mu\text{S/cm}^2$, and $\tau_e = 1.5$ ms.

As for the conductance-based LIF model, we use spike trains as input for the conductance-based HH neurons. We derived the membrane potential

using Euler integration with a step width of 0.05 ms for the HH neurons. The sequence of output action potentials of the HH model was represented in time bins of 1 ms.

2.4 Multitaper Method. The usual way of estimating the frequency content of a signal is by taking the Fourier spectrum (periodogram). If the signal $x(t)$ has a stochastic character, the variance of the spectral estimates in the Fourier transformed signal may be considerable. This is particularly important if we are dealing with the coherence of two stochastic spike series. This is not solved by taking a signal with a longer duration since a longer time signal gives rise to a higher spectral resolution in the Fourier transformed signal but does not decrease the variance of each point in the frequency spectrum.

To solve this problem, the multitaper estimation procedure was introduced (see Thomson, 1982; Mitra & Pesaran, 1999). The key idea behind the Welch method and the multitaper method is that a physiological signal has no discontinuities in the frequency spectrum and that the variability in the estimate of a signal can be reduced by smoothing in the frequency domain. The multitaper method achieves this by optimizing the minimum of bias and variance of the estimate. This involves the use of multiple orthonormal data tapers, which provide a local eigenbasis in frequency space for finite-length data sequences. A simple example of the method is given by the direct multitaper spectral estimate $S_{MT}(f)$ of a discrete time series signal x_t with $t = n\Delta t$ and $n \in 1, 2, \ldots, N$ defined as the average over individual tapered spectral estimates,

$$S_{MT}(f) = \frac{1}{N} \sum_{k=1}^{K} \mid \tilde{x_k}(f) \mid^2 \tag{2.26}$$

where

$$\tilde{x_k}(f) = \sum_{1}^{N} w_t(k) x_t \exp(-2\pi i f t). \tag{2.27}$$

Here $w_t(k)$ $(k = 1, 2, \ldots, K)$ are K orthogonal taper functions with appropriate properties. Let $w_k(k, W, N)$ be the kth taper of length N and frequency bandwidth parameter W. This forms an orthogonal basis set for sequences of length N, characterized by a bandwidth W. The important feature of these sequences is that for a given bandwidth parameter W and taper length N, $K = 2NW - 1$ sequences out of a total of N each have their energy effectively concentrated within a range $2W$ in frequency space. This range can be shifted from $[-W, W]$ centered around zero frequency to any nonzero center frequency interval

$[f_0 - W, f_0 + W]$ by simply multiplying by the appropriate phase factor $\exp(2\pi f_0 t)$. The product of the number N of samples in the signal and the bandwidth W of the spectral estimator (NW) is used to balance between variance and resolution of the power spectral density estimation. In this article, we use a simple set of orthonormal sine tapers $\{\omega_{t,k} : t = 1, \ldots, N; k = 0, \ldots, N-1\}$ (McCoy, Walden, & Percival, 1997). The kth taper is given by

$$\omega_{t,k} = \sqrt{\frac{1}{N+1}} \sin\left(\frac{(k+1)\pi t}{N+1}\right). \tag{2.28}$$

For our analysis, we used signals of length 0.512 s and the first $K = 2NW - 1$ tapers, which gave $K = 6$. This means that the bandwidth W of the spectral estimator is 6.83 Hz. The frequency bin width is $f_s/\text{nfft} = 1.95$ Hz, with sampling frequency f_s (1000 Hz) and where nfft is the number of data in the FFT (512).

2.5 Neurophysiology

2.5.1 Surgery. Experiments were performed on two male *Macaca mulatta*, weighting 8 to 11 kg. Each monkey was surgically implanted with a head post, a scleral eye coil, and a recordings chamber. Surgery was conducted under aseptic conditions with isofluorane anesthesia. Antibiotics and analgesics were administered after the operation. The skull remained intact during the surgery. Subsequently, small holes (5 mm in diameter) were drilled within the recording chamber under ketamine anesthesia and xylazine analgesic. All experimental procedures were performed in accordance with the National Institutes of Health guidelines and approved by the National Institute of Mental Health Intramural Animal Care and Use Committee.

2.5.2 Recording-Technique. Neuronal recordings were made through the surgically implanted chamber overlying area V4. Recordings were made from two hemispheres in two monkeys. Four to eight tungsten microelectrodes (Frederick Haer and Co., Brunswick, ME) were inserted through the intact dura mater by means of a hydraulic microdrive (Frederick Haer) mounted to the recording chamber. The electrodes had tip impedances of one to two MΩ and were separated by 650 or 900 μm. Each electrode was advanced separately at a very slow rate (1.5 mm/s) to minimize suppression artifacts (dimpling) resulting from the deformation of the cortical surface by the electrode. Data amplification, filtering, and acquisition was done with a multichannel acquisition processor (MAP) system from Plexon Incorporated (Dallas, TX). The signal from each electrode was passed through a headstage with unit gain and an output impedance of 240 Ω. It

was then split to separately extract the spike and the LFP components. For spike recordings, the signals were filtered with a passband of 100 to 8000 Hz, further amplified and digitized with 40 kHz. A threshold was set interactively, and spike waveforms were stored for a time window from 150 μs before to 700 μs after threshold crossing. The threshold clearly separated spikes from noise but was chosen to include multi-unit activity. Off-line, we performed a principal component analysis of the waveforms and plotted the first against the second principal component. Those waveforms that corresponded to artifacts were excluded. For multi-unit analyses, all other waveforms were accepted. For single-unit analyses, only clearly isolated clusters of high-amplitude spikes were accepted. For all further analyses involving spikes, only the times of threshold crossing were kept and downsampled to 1 kHz. For LFP recordings, the signals were filtered with a passband of 0.7 to 170 Hz, further amplified, and digitized at 1 kHz.

Each electrode was lowered separately until it recorded visually driven activity. Once this had been achieved for all electrodes, we fine-tuned the electrode positions to optimize the signal-to-noise ratio of the multiple spike recordings and obtain as many isolated single units as possible. Since the penetration was halted as soon as clear visually driven activity was obtained, most of the recordings were presumably done from the superficial layers of the cortex.

2.5.3 Behavioral Paradigm and Visual Stimulation. Stimuli were presented on a 17 inch CRT monitor 0.57 m from the monkeys' eyes that had a resolution of 800 $\times$ 600 pixel and a screen refresh rate of 120 Hz noninterlaced. Stimulus generation and behavioral control were accomplished with the CORTEX software package (http://www.cortex.salk.edu/). A trial started when the monkey touched a bar mounted in front of him; 250 ms later, a fixation point appeared at the center of the screen. When the monkey brought his gaze within 0.7 degree of the fixation spot for at least 1000 ms, stimulus presentation commenced. The task of the monkey was to fixate the fixation target while a drifting sine wave grating was presented within the receptive field. He had to release the bar between 150 and 650 ms after a change in stimulus color of the sine-wave grating. That change in stimulus color could occur at an unpredictable moment in time between 500 and 5000 ms after stimulus onset. With this task, we ensured that the monkey was constantly monitoring the grating that induced the recorded neuronal activity while fixating the fixation target. The first 300 ms after stimulus onset were discarded in order to avoid strong stimulus-onset-related transients, and the rest of the data were analyzed until the time of the color change. Successful trial completion was rewarded with four drops of diluted apple juice. If the monkey released the bar too early or moved his gaze out of the fixation window, the trial was immediately aborted and followed by a time-out.

3 Results

In this section, we describe coherence estimates between various signals. We always first analyze the spike-field coherence followed by the spike-spike coherence for both single-unit and multi-unit activity. The simulation results will be shown first for the Poisson model neurons (small circles in Figure 1), followed by the conductance-based neurons (LIF and HH; big circles in Figure 1). We end this section with the results of the spike-field and spike-spike coherences of experimental data. Finally, we compare an analysis without and with the use of multitaper techniques.

3.1 Simulation Results of the Poisson Model. The top panels of Figure 2 show the predicted (dashed line) and the simulated (solid line) coherence between the LFP and single-unit activity (see Figure 2A) and between LFP and multi-unit activity (see Figure 2B) for the Poisson neurons. In both cases, there is a good match between the simulated and predicted spike-field coherence functions.

The "predicted" coherence functions were obtained using the Fourier transform of the normalized covariance function $\rho(\tau)$ of the LFP. Since the LFP had a finite duration, $\rho(\omega)$ has noisy fluctuations that are evident in the "predicted" coherence function of Figure 2. The coherence is larger for the multi-unit activity in Figure 2B than for the single-unit activity in Figure 2A. The ratio between the peak coherence for multi-unit versus single-unit activity ($0.37/0.12 = 3.08$) is in agreement with the square root of the number of neurons ($\sqrt{10} = 3.16$) that contributes to the multi-unit activity (see Equations 2.10 and 2.13). One could argue that the larger coherence for the multi-unit case could be due to the fact that the multi-unit recording with 10 (simultaneously measured) single-unit signals contains 10 times more action potentials. In order to correct for this, the single-unit signal in our simulations was 10 times longer than the multi-unit signal such that the number of action potentials was the same in both signals.

Figure 2C shows the simulated (solid line) and predicted (dashed line) spike-spike coherence for single-unit activity for the Poisson neurons. Figure 2D shows the same results for multi-unit activity. The simulated and predicted coherence are in agreement for the single-unit and multi-unit data.

The spike-spike coherence for multi-unit activity increases linearly with the number of units ($m = 10$) in the multi-unit recording for the spike-spike coherence as long as $m << 1/(\lambda \Delta t)$. This is shown by the peaks of the coherences in Figures 2C and 2D (0.015 versus 0.14).

The spike-spike coherence differs from the spike-field coherence in two aspects (see equations 2.17 and 2.13). The first difference concerns the factor m versus $\sqrt{m}$ for spike-spike versus spike-field coherence. The second difference is that the spike-field coherence is proportional to $\sqrt{\rho(\omega)}$, whereas

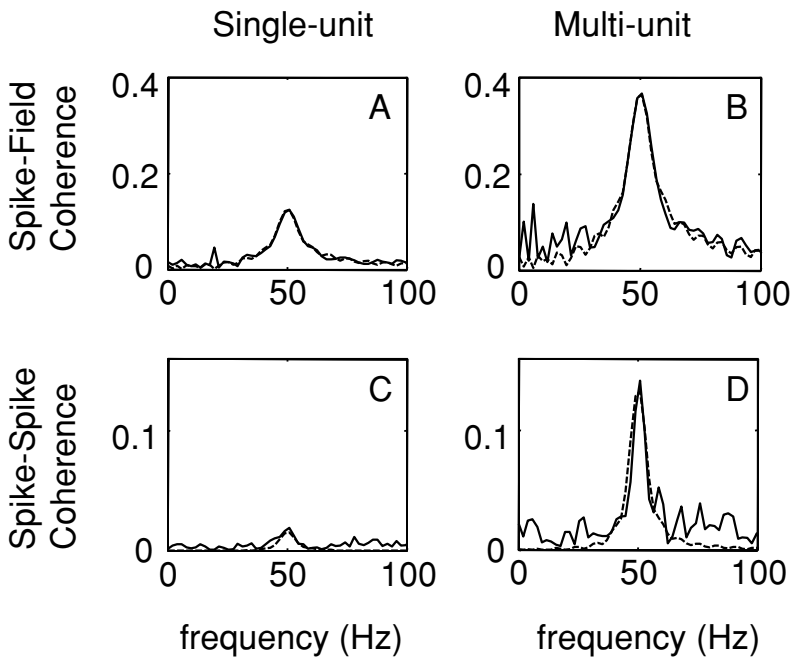

Figure 2: Predicted (dashed lines) and simulated (solid lines) coherence functions for LFP and single-unit (A,C) and multi-unit (B,D) signals for the Poisson neurons (see Figure 1). Parameter values used were $\lambda = 20$, $\sigma = 20/12$, $N_c = 0.4$, and a simulation duration of 512 s. The number of action potentials in the multi-unit and in the single-unit signals is about 20.480 spikes. (A) The coherence between LFP and single-unit activity. (B) The coherence between LFP and multi-unit activity shows a peak near 50 Hz, which is larger than that for single-unit activity shown in *A*. (C) The predicted and simulated coherences between two single-unit activities. (D) The predicted and simulated coherence function between two multi-unit activities.

the spike-spike coherence is proportional to the normalized covariance function of the common rate fluctuations, $\rho(\omega)$. Since $0 <\mid \rho(\omega) \mid < 1$, $\rho(\omega)$ is smaller and more narrow than $\sqrt{\rho(\omega)}$.

Both aspects are reproduced in Figure 2. The peak value of the spike-spike coherence (see figure 2D: 0.14) is approximately the square root of the maximum peak value of the spike-field coherence (see Figure 2B: 0.37).

Equations 2.10, 2.13, 2.15, and 2.17 for the spike-field and spike-spike coherence do not depend on the duration of the LFP and spike series. Therefore, the expectation value for the coherence functions will not change if the duration of the single-unit recordings increases. The only effect of a longer duration of the spike recording is a reduction of the noise in the coherence

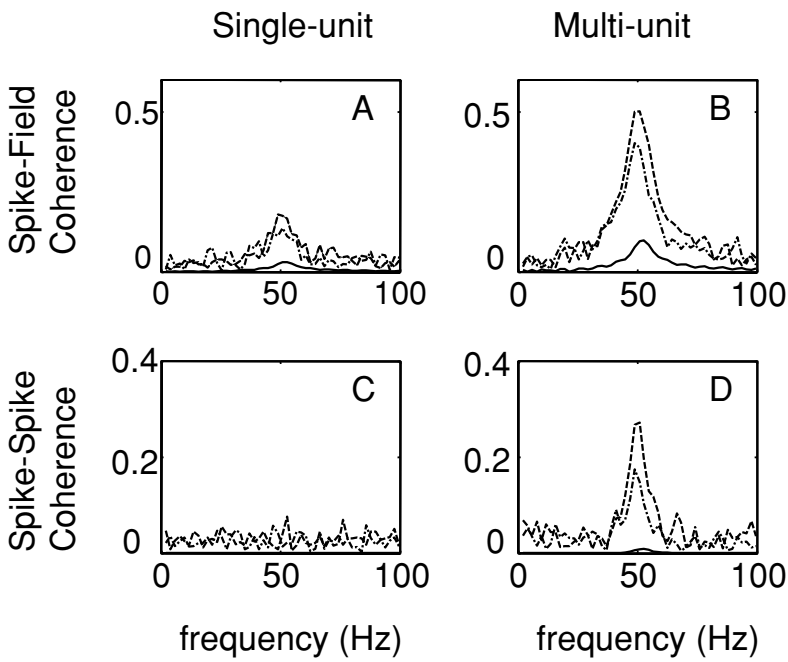

Figure 3: Coherences between LFP and single- and multi-unit activities for the conductance-based LIF model (dashed-dotted lines), the HH model (dashed lines), and the predictions for the Poisson model (solid line) according to Equations 2.10, 2.13, 2.15, and 2.17. Parameter values used were $\lambda = 20$, $\sigma = 20/12$, $N_c = 0.4$, and a simulation duration of 512 s. (A) Spike-field coherence estimates for single-unit activity. (B) Spike-field coherence estimates for multi-unit activity. (C) Spike-spike coherence estimates for single-unit activity. (D) Spike-spike coherence estimates for multi-unit activity.

function. Therefore, a smaller coherence for single-unit recording relative to multi-unit recording cannot be compensated by a longer recording time for the single-unit recordings.

3.2 Simulation Results for the Conductance-Based LIF and HH Model. Figure 3 shows the spike-field and the spike-spike coherences for single-unit and multi-unit recordings for the conductance-based LIF neuron (dashed-dotted line), the conductance-based HH neuron (dashed line) model, and the predictions for the Poisson model (solid line) according to equations 2.10, 2.13, 2.15, and 2.17, all with $\sigma = 20/12$. The parameters were chosen in such a way that the mean firing rate was the same for the Poisson neuron, the LIF, and the HH neurons. Figure 3A (3B) shows the coherence between the LFP and single-unit (multi-unit) activity. For both the

single-unit and multi-unit recordings, the spike-field coherence estimate shows a significant peak near 50 Hz. The peak value of the spike-field coherence estimates for multi-unit recording in Figure 3B is considerably higher than the peak value for the single-unit recording in Figure 3A. The spike-field coherence estimates for the LIF and HH network have much higher values than the spike-field estimates of the Poisson network. The ratio of the two peak spike-field coherence values (multi-unit/single-unit) is smaller than the square root of the number m ($m = 10$; $\sqrt{m} = 3.16$) of neurons active in the multi-unit.

Figure 3C (3D) shows the coherence between two single-unit (multi-unit) recordings. For the single-unit recordings, no significant peak near 50 Hz is visible. The predicted coherence for the Poisson model is small and lies almost on the x-axis, with a small (hardly visible) peak near 50 Hz for the multi-unit activity. For multi-unit activity (see Figure 3D), a significant peak near 50 Hz is visible.

The peak coherence is larger for the LIF neuron and the HH model than for the Poisson neuron, for both the spike-field coherence and the spike-spike coherence. The question is whether the higher coherence values for the LIF and HH neuron are due to the dynamics of these neurons or due to the different type of input (continuous LFP signal for the Poisson neurons versus spike input to the LIF and HH neuron). In order to investigate this, we have calculated the coherence between the spike input to the LIF and HH neuron (i.e., the sum of spike series of the Poisson neurons) and their output. These coherence values are much higher than the coherence between the input and the output of a Poisson neuron, with the same input as the LIF and HH neuron. Therefore, we conclude that the higher coherence values of the LIF and HH neuron are the result of the dynamic properties of those neuron types.

3.3 Data from Monkey Visual Cortex. As a final test of the significance of the model simulations, we have analyzed data obtained in monkey visual cortex (Fries, Reynolds, et al., 2001). The data consisted of single- and multi-unit activity and local field potential activity recorded simultaneously in area V4 of the awake macaque monkey.

Figure 4A shows the coherence between the measured LFP and the single-unit signal, which contains 15,371 spikes. The dashed-dotted lines indicate the 95% confidence levels of the coherence estimates, calculated with 130 bootstraps, and the solid line is the average of the bootstrap replications. For a multi-unit recording with a similar number ($n = 16{,}031$) of spikes and thus a shorter duration, the spike-field coherence is shown in Figure 4B. In both Figures 4A and 4B, there is a peak in spike-field coherence near 50 Hz. For multi-unit activity (sum of approximately eight single-unit activities), this peak is significantly higher than that for single-unit activity. Figure 4C shows the spike-field coherence for a multi-unit signal with a duration equal to the duration of the single-unit recording used for

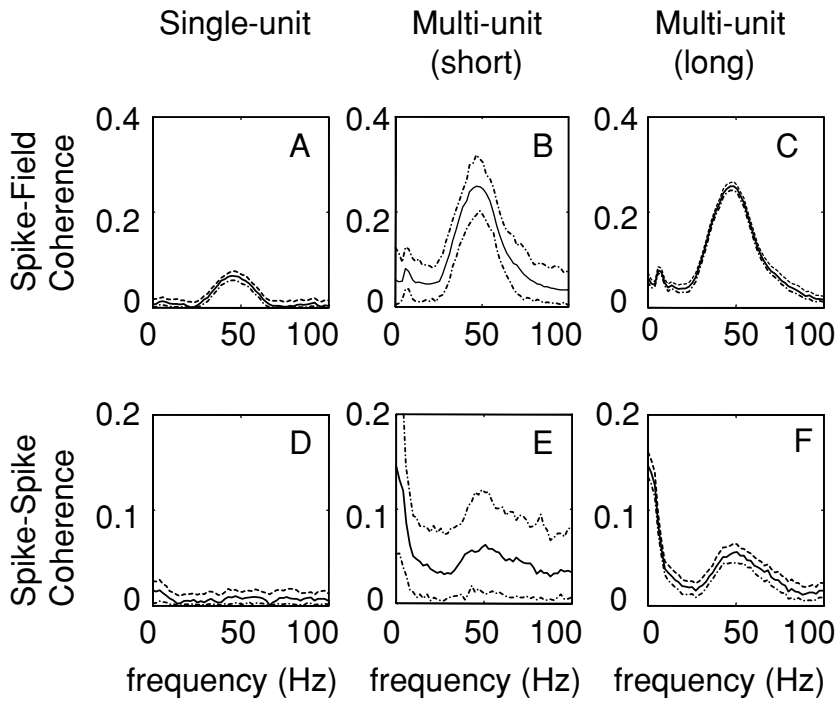

Figure 4: Coherences between LFP and single-unit or multi-unit recordings (experimental data), using the multitaper method. For the multitaper method, we used a set of six orthonormal sine tapers. The 95% confidence level (dashed-dotted lines) is obtained using 130 bootstraps. (A) Coherence between LFP and single-unit recording with 15,371 spikes. (B) Coherence between LFP and multi-unit recording, with 16,031 spikes. (C) Coherence between LFP and multi-unit recording, with 668,766 spikes. (D) Coherence between two single-unit recordings. The variance in coherence is too large to detect a significant peak near 50 Hz. (E) Coherence between two multi-unit recordings. (F) Coherence between two multi-unit recordings, with durations equal to those of the single-unit recordings used in Figure 4A. Compared to Figure 4E, the 95% confidence regime has been reduced.

Figure 4A. The coherence estimate, including the 95% confidence level, in Figure 4C, is entirely within the 95% regime shown in Figure 4B. Figures 4B and 4C illustrate that increasing the duration of a spike recording improves the signal-to-noise ratio but does not change the expectation value of the coherence function.

The spike-spike coherence for single-unit signals in Figure 4D does not show a significant peak near 50 Hz. Neither does the spike-spike coherence for multi-unit signals if the analyzed time period is shortened such that

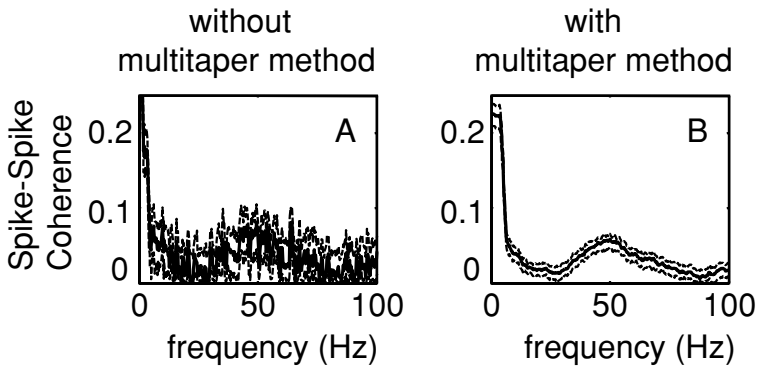

Figure 5: The effect of the multitaper method on the spike-spike coherence between multi-units. (A) The spike-spike coherence estimate of experimental data without the use of multitapers. There is no significant peak near 50 Hz. (B) Using the multitaper method with sine tapers resulted in a significant peak and a significant reduction of the 95% regime.

the number of spikes is the same as in the longer single-unit recording in Figure 4E. The coherence values for the multi-unit signals in Figure 4E are larger than for single unit signals shown in Figure 4D. However, the 95% confidence regime is relatively large. Figure 4F shows the spike-spike coherence for multi-unit signals with duration equal to the duration of the single-unit activities used in Figure 4D. The coherence function in Figure 4F shows a significant peak near 50 Hz. The signal-to-noise ratio is considerably better than in Figure 4E. The results shown in Figure 4 are typical for the spike signals that were obtained in the study by Fries, Reynolds, et al. (2001).

All coherence estimates of Figure 4 were obtained with the multitaper method as described in the section 2. Each trial was cut into equally long segments of 512 ms such that the number of tapers was constant. In fact, this is a combination of the Welch method and the multitaper technique.

As an alternative to using the Welch method with equally long time segments, one could use the multitaper technique for the analysis of spike signals, which in general each have a different duration. Since the trial durations are different, so is the number of samples in each trial. In order to keep the frequency of smoothing in the frequency domain ($2W$) constant, the number of tapers given by $K = 2NW - 1$ is different for each trial. Since averaging over power spectra of different trials requires that the frequency resolution of the spectra be the same for all trials, all signals (after application of the tapers) are made of equal duration by adding zeros (zero padding). Now the average FFTs of the cross and covariance functions can be derived for the coherence functions.

Figure 5A shows the spike-spike coherence estimate of experimental multi-unit spike trains without the use of multitapers and without using the Welch method. The frequency resolution in Figure 5 is much higher than that in Figure 4F because the number of data points in the frequency domain is eight times larger. The variance in the coherence estimate is large, and no significant peak is visible near 50 Hz. By applying the multitaper method with $W = 5$ Hz, the variance is reduced, and a significant peak near 50 Hz is visible in the same data (see Figure 5B).

4 Discussion

The coherence between neuronal signals (e.g., EEG, MEG, two spike trains) or between neuronal input (e.g., a local field potential) and neuronal output is generally considered as an important measure for synchronization or temporal locking. The main result of this study is that the coherence reaches higher values when multi-unit spike activity is used instead of single-unit activity. This cannot be overcome by extending the recording time of the single-unit signal. The latter only improves the signal-to-noise ratio (SNR) of the coherence. The SNR can also be improved by using multitaper techniques or by using the Welch method. Experimental data obtained in monkey V4 could be reproduced by simulations. Our results illustrate the significance of multi-unit activity over single-unit activity and provide new insights for the interpretation of multi-unit activity and for the interpretation of coherence estimates using oscillatory activity such as β-oscillations and γ-oscillations in cognitive neuroscience studies. Our results will be discussed in more detail below.

Although many studies have investigated the firing behavior of Poisson neurons and integrate-and-fire neurons for partially correlated and uncorrelated input (for an overview, see Salinas & Sejnowski, 2001), most studies have focused on the mean firing rate and the coefficient of variation (see, e.g., Feng & Brown, 2000; Stroeve & Gielen, 2001; Salinas & Sejnowski, 2000, 2002; Kuhn, Aertsen, & Rotter, 2004). The coefficient of variation is an important parameter to understand the temporal structure of spike trains, but this parameter itself cannot provide insight into the temporal correlation of the action potential signals of different neurons receiving partially correlated input. As far as we know, this study is the first to give analytical expressions and results of computer simulations for the coherence between local field potential and neuronal firing and for the coherence between spike signals for neurons receiving (partly) correlated input.

In this study, we investigated the relations between spike-field and spike-spike coherences for single-unit and multi-unit activity. Analytical expressions (see equations 2.10, 2.13, 2.15, and 2.17) showed that the spike-field coherence values are higher than the spike-spike coherence values and that the coherences are larger for multi-unit recordings than for single-unit recordings. Although we could derive analytical expressions for the

coherence between input and spike output only for the Poisson neurons, simulations show qualitatively similar results for an ensemble of conductance-based LIF neurons or HH neurons.

For Poisson neurons, the spike-spike coherence should be proportional to the square of the spike-field coherence. This was confirmed by simulations (compare Figures 2B and 2D) where the spike-spike coherence equals the square of the spike field coherence for the Poisson model. Figures 3A, 3B, and 3D show similar results for the conductance-based LIF model and the Hodgkin-Huxley neuron model. The full width at half maximum and the amplitude of the peak are smaller for the spike-spike than for the spike-field coherence, as expected in case the spike-spike coherence is proportional to the square of the spike-field coherence, which has values between zero and one. However, coherence values were typically larger for the conductance-based LIF and Hodgkin-Huxley neuron than for the Poisson neuron. This is due to the characteristic dynamic properties of the neuron models.

Our results demonstrate that multi-unit activity gives significantly higher estimates for the coherence than single-unit activity even if the number of action potentials in both signals is the same (see Figures 4A, 4B and 4D, 4E). This is partially due to the fact that the mean firing rate is typically higher in a multi-unit recording than in a single-unit recording and the modulations in firing rate are larger. Equations 2.10 and 2.13 show that the coherence decreases with the square root of firing rate (proportional to λ) but increases linearly with modulation depth σ. Since firing rate and modulation depth increase proportionally when adding single-unit signals, the coherence will effectively increase with the number of single-unit contributions in a multi-unit signal.

Several studies have reported a lack of evidence for synchronized neuronal activity; see, for example Tovee and Rolls (1992) in the inferior temporal visual cortex and Luck et al. (1997) who did not observe clear synchronization in neuronal responses in V2 and V4. This is in contrast to findings by Fries, Reynolds, et al. (2001). Our results indicate that the explanation for these apparently contradictory findings may be related to the techniques used to analyze the neuronal data. In Figure 3C the spike-spike coherence between single-unit signals is small and disappears in the relatively high variance of the estimate. Simulations with larger values of σ (larger modulations of the stimulus) showed a clear, small, and narrow peak near 50 Hz. However, the signal-to-noise ratio increases to plausible levels only for unrealistically high modulations of the input. Therefore, the variance in experimental data should be reduced by using dedicated data analysis techniques like the multitaper method (see Figures 4 and 5). Our simulations were done for data segments of equal duration (512 ms) and with a constant number ($K = 6$) of tapers repeated over many time segments. This results in smoothing of the frequency spectrum by averaging over many signals.

In electrophysiological experiments, the recording duration will vary by experiment and will typically be much longer than 512 ms. Therefore, Fries, Reynolds, et al. (2001) used a different number of tapers for each recording signal, such that smoothing was done over the same frequency window ($2W =$ constant) for all experimental data. Since the duration of their recordings was typically much longer than 512 ms, the longer duration gives more samples in the time domain, which results in a higher resolution in the frequency domain. This is illustrated in Figure 5. Their result shows a higher resolution in the frequency domain but averaging over a smaller number of signals. Effectively the result is the same: the reduction of smoothing by the smaller number of signals is compensated by smoothing by the tapers over a larger number of samples in the frequency domain. However, note that the multitaper method with Slepian sequences as tapers is optimal among quadratic estimators because of the good concentration properties of Slepian sequences (see Percival & Walden, 2002). The lack of optimality of the Welch estimates means that it is a more biased estimate than the multitaper estimate with Slepian sequences, the variance and the frequency resolution being equal. The bias will grow as the size of the windows becomes smaller.

Acknowledgments

We thank Robert Desimone and John Reynolds for supporting the experimental recordings.

References

Baker, S. N., Pinches, E. M., & Lemon, R. N. (2003). Synchronization in monkey cortex during a precision grip task. II. Effect of oscillatory activity on corticospinal output. *J. Neurophysiol., 89*, 1941–1953.

Brown, E. N., Kass, R. E., & Mitra, P. P. (2004). Multiple neural spike train data analysis: State-of-the-art and future challenges. *Nature Neuroscience, 7*, 456–461.

Buzsáki, G. (2004). Large-scale recording of neuronal ensembles. *Nature Neuroscience, 7*, 446–451.

Engel, A. K., Fries, P., & Singer, W. (2001). Dynamic predictions: Oscillations and synchrony in top-down processing. *Nature Review Neuroscience, 2*(10), 704–716.

Feng, J., & Brown, D. (2000). Impact of correlated inputs on the output of the integrate-and-fire model. *Neural Computation, 12*, 671–692.

Fries, P., Neuenschwander, S., Engel, A. K., Goebel, R., & Singer, W. (2001). Rapid feature selective neuronal synchronization through correlated latency shifting. *Nature Neuroscience, 4*, 194–200.

Fries, P., Reynolds, J. H., Rorie, A. E., & Desimone, R. (2001). Modulation of oscillatory neuronal synchronization by selective visual attention. *Science, 291*, 1560–1563.

Fries, P., Schröder, J. H., Roelfsema, P. R., Singer, W., & Engel, A. K. (2002). Oscillatory neuronal synchronization in primary visual cortex as a correlate of stimulus selection. *J. Neurosci., 22*, 3739–3754.

Jarvis, M. R., & Mitra, P. P. (2001). Sampling properties of the spectrum and coherence of sequences of action potentials. *Neural Computation, 13*, 717–749.

Kreiter, A. K., & Singer, W. (1996). Stimulus-dependent synchronization of neural responses in the visual cortex of awake macaque monkey. *J. Neurosci., 16*(7), 2381–2396.

Kuhn, A., Aertsen, A., & Rotter, S. (2004) Neuronal integration of synaptic input in the fluctuation-driven regime. *J. Neurosci., 24*, 2345–2356.

Luck, S. J., Chelazzi, L., Hillyard, S. A., & Desimone, R. (1997). Neural mechanisms of spatial selective attention in areas V1, V2, and V4 of macaque visual cortex. *J. Neurophysiol., 77*(1), 24–42.

Marmarelis, P. Z., & Marmarelis, V. Z. (1978). *Analysis of physiological systems: The white-noise approach*. New York: Plenum Press.

McCoy, E. J., Walden, A. T., & Percival, D. B. (1997). Multitaper spectral estimation of power law processes. *IEEE Trans. on Sign. Proc., 46*(3), 655–668.

Mitra, P. P., & Pesaran, B. (1999). Analysis of dynamic brain imaging data. *Biophys. J., 76*(2), 691–708.

Percival, D. B., & Walden, A. T. (2002). *Spectral analysis for physical applications: Multitaper and conventional univariate techniques*. Cambridge: Cambridge University Press.

Pesaran, B., Pezaris, J. S. Shahani, M., Mitra, P. P., & Andersen, R. A. (2002). Temporal structure in neuronal activity during working memory in macaque parietal cortex. *Nature Neuroscience, 5*, 805–811.

Rolls, E. T., Franco, L., Aggelopous, N. C., & Reece S. (2003). An information theoretic approach to the contributions between the firing rates and the correlations between the firing of neurons. *J. Neurophysiol., 89*, 2810–2822.

Salinas, E., & Sejnowski, T. (2000). Impact of correlated synaptic input on output firing rate and variability in simple neuronal models. *J. Neurosci., 20*, 6193–6209.

Salinas, E., & Sejnowski, T. (2001). Correlated neuronal activity and the flow of neural information. *Nat. Rev. Neurosci., 2*, 539–550.

Salinas, E., & Sejnowski, T. J. (2002). Integrate-and-fire neurons driven by correlated stochastic input. *Neural Computation, 14*, 2111–2155.

Singer, W., & Gray, C. M. (1995). Visual feature integration and the temporal correlation hypothesis. *Ann. Rev. Neurosci., 18*, 555–586.

Stroeve, T., & Gielen, C. (2001). Correlation between uncoupled conductance-based integrate-and-fire neurons due to common and synchronous presynaptic firing. *Neural Computation, 13*, 2005–2030.

Thomson, D. J. (1982). Spectrum estimation and harmonic analysis. *Proc. IEEE., 70*, 1055–1096.

Tovee, M. J., & Rolls, E. T. (1992). Oscillatory activity is not evident in the primate temporal visual-cortex with static stimuli. *NeuroReport, 3*(4), 369–372.

Received June 30, 2005; accepted February 17, 2006.